

Forensics of Subhalo-Stream Encounters: The Three Phases of Gap Growth

Denis Erkal^{1*} & Vasily Belokurov¹

¹*Institute of Astronomy, Madingley Road, Cambridge, CB3 0HA, UK*

10 June 2015

ABSTRACT

There is hope to discover dark matter subhalos free of stars (predicted by the current theory of structure formation) by observing gaps they produce in tidal streams. In fact, this is the most promising technique for dark substructure detection and characterization as such gaps grow with time, magnifying small perturbations into clear signatures observable by ongoing and planned Galaxy surveys. To facilitate such future inference, we develop a comprehensive framework for studies of the growth of the stream density perturbations. Starting with simple assumptions and restricting to streams on circular orbits, we derive analytic formulae that describe the evolution of all gap properties (size, density contrast etc) at all times. We uncover complex, previously unnoticed behavior, with the stream initially forming a density enhancement near the subhalo impact point. Shortly after, a gap forms due to the relative change in period induced by the subhalo’s passage. There is an intermediate regime where the gap grows linearly in time. At late times, the particles in the stream overtake each other, forming caustics, and the gap grows like \sqrt{t} . In addition to the secular growth, we find that the gap oscillates as it grows due to epicyclic motion. We compare this analytic model to N-body simulations and find an impressive level of agreement. Importantly, when analyzing the observation of a single gap we find a large degeneracy between the subhalo mass, the impact geometry and kinematics, the host potential and the time since flyby.

Key words: cosmology: theory - dark matter - galaxies: haloes - galaxies: kinematics and dynamics - galaxies: structure

1 INTRODUCTION

Let us recall one strong and imminently testable prediction of the modern Cosmology: in the early Universe, Dark Matter (DM) starts collapsing first and ends up arranging itself into a hierarchy of dense clumps of all sizes (e.g. White & Rees 1978). For example, by redshift $z = 0$, a DM halo with a Milky Way mass is anticipated to contain hundreds of thousands of subhalos (e.g. Diemand et al. 2008; Springel et al. 2008), some as massive as $10^9 M_\odot$, but the majority too insignificant to kick-start star-formation, and, hence, completely devoid of light. Nonetheless, detecting these dark halos through their gravitational effects is feasible with existing technology and quantifying their abundance will shed light on the nature of Dark Matter.

Two promising experimental setups have been put forward, both to do with the minuscule perturbations the dark substructure inflicts on test particle orbits in the gravitational potential in question. In one case, the role of such test particles is played by photons traveling in the density field of a massive galaxy acting as a gravitational lens. Intervening dark substructure then would either cause flux anomalies in the lensed images if the source is a quasar (e.g.

Dalal & Kochanek 2002) or send ripples through the lensed arcs if the source is extended (e.g. Vegetti et al. 2010). Alternatively, Galactic stellar streams can be used as bundles of test particles to probe the lumpiness of DM distribution. During close flybys, the invisible subhalos ought to ruffle the orbits of stars in the stream, imprinting characteristic small-scale features in their density profile. With time, such perturbation will grow, revealing a sizeable density gap. There exists, therefore, a crucial difference between the two experiments: the time dependence of the stream gap growth spells out increased detectability of the DM substructure.

Evidently, if the observations of the tidal streams are to be used to infer the mass function of the DM subhalos, it is important to understand the time evolution of the induced density fluctuations. However, the idea of the halo-stream interaction is relatively new (e.g. Ibata et al. 2002; Johnston, Spergel & Haydn 2002), and, while the overall picture has been painted with help of numerical simulations (e.g. Siegal-Gaskins & Valluri 2008; Carlberg 2009; Yoon, Johnston & Hogg 2011; Carlberg 2012), the stream dynamics due to flybys has remained unexplained until recently when Carlberg (2013) laid down the basic equations governing the stream gap formation. In this work, we will follow a similar strategy and consider the gaps created in a stream on a circular orbit around an arbitrary spherical potential.

* derkal@ast.cam.ac.uk

Taking advantage of this stripped-down approach, we can develop an in-depth insight into the complex metamorphosis of the stream density fluctuations created during encounters with dark halos. We show that, despite the rich dynamics that ensues, many properties of the stream gaps (e.g. gap size and density in the center of the gap) can be solved for analytically. More generally, it is actually possible to write a parametric function for the density profile of the stream at all times. Importantly, our model is shown to accurately describe the behaviour of realistic tidal streams generated in N-body simulations.

Observationally, impressive progress has been made recently in both detecting cold stellar streams in the Galaxy (e.g. Odenkirchen et al. 2003; Belokurov et al. 2006; Grillmair & Dionatos 2006; Bonaca, Geha & Kallivayalil 2012; Koposov et al. 2014; Bernard et al. 2014) as well as quantifying the presence of the density gaps in some of them (Carlberg, Grillmair & Hetherington 2012; Carlberg & Grillmair 2013). Interpreting these observations, the intuition established so far utters that the gap size encodes predominantly the mass of the dark subhalo which wreaked the damage (e.g. Yoon, Johnston & Hogg 2011). Our analysis demonstrates that such portrayal of the results of the halo-stream interaction is, unfortunately, too optimistic. The inference based on the gap size alone appears to be deeply degenerate as it is controlled by several poorly constrained variables. As we elucidate, it is possible to produce the same size gap in a stream by altering the dark halo mass, the underlying host potential, the parameters of the impact, or simply by observing the stream at a different epoch.

Fortunately, the dynamical age of the stream gap can be gleaned from the details of the density profile in its vicinity. This is because the gap growth proceeds in a particular sequence of phases, each described by a specific density contrast (and its temporal evolution), the onset timescale, and the rate of gap growth. For each of the three phases of the stream gap growth, the compression, the expansion, and the caustic phase, our paper provides the corresponding analytic formulae. We, therefore, build a clear and comprehensive framework which can be used to decipher the dark halo ballistics.

This paper is organized as follows. In Section 2, we begin with a qualitative description of how stream gaps grow. We follow this with a rigorous derivation in Section 3. In Section 4, we compare this model with idealistic N-body simulations of streams on circular orbits, as well as a realistic N-body simulation with a stream generated by tidally disrupting a globular cluster. In Section 5, we examine the degeneracy in extracting physical parameters from gap profiles. In Section 6 we discuss how the results can be generalized and how these results can be used to shed light on the results of previous works. Finally, we conclude in Section 7.

2 QUALITATIVE EXPLANATION

Before we present a rigorous derivation of how stellar density gaps evolve in the toy stream model in Section 3, let us first give a simple, intuitive explanation. For guidance, a visual summary of the important stages of the process is also presented in Figure 1.

Let us start with an unperturbed stellar stream on a circular orbit around an arbitrary spherical potential. By restricting the analysis to this simple case, we will be able to solve the gap growth analytically. Bear in mind, however, that the qualitative picture presented in this work is quite general and will hold for realistic streams, i.e. those that have a distribution of energy and angular

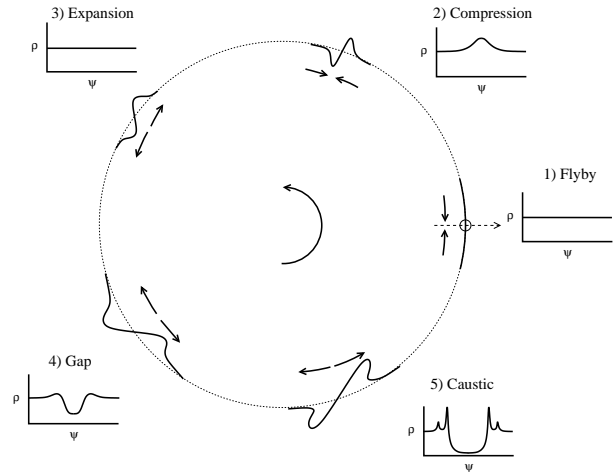


Figure 1. A cartoon of gap formation and evolution. The dotted line delineates the orbit of the stream and the black lines show a segment of the stream near the point of closest approach. The graphs show the density along the stream for an observer in the center of the galaxy where ψ is the angle on the sky. The arrow in the center shows the orbital direction of the stream and the arrows near the stream show whether the stream is compressing or expanding. Before impact, the stream has a uniform density (1). Shortly after, the stream is compressed since the subhalo kicks the particles towards the point of closest approach (2). The kicks also change the orbital period of particles in the stream: particles kicked along their orbital direction have a longer period which will cause them to fall behind the impact point and vice-versa. As a result, the compression is reversed (3) and eventually a gap forms (4). This expansion continues and at late times the stream particles overtake each other, forming caustics (5). See Fig. 7, Fig. 8, and Fig. 9 for examples of the same behavior in N-body simulations.

momenta in their debris (see Sec. 4.2), as well as for eccentric orbits (see Sec. 6).

As a subhalo passes near (or through) the stream, its main effect is to pull stream particles towards the point of closest approach (1 of Fig. 1). For a wide range of encounters of interest, these subhalo tugs are instantaneous as compared to the stream’s orbital timescale, and therefore the application of the impulse approximation is justified. The kicks imposed by a massive perturber can be decomposed into three components: perpendicular to the stream’s orbital plane, along the radial direction from the host, and along the orbit. Kicks perpendicular to the orbital plane tilt the plane slightly which causes particles to oscillate with respect to the original plane. Radial kicks rotate the orbit in the orbital plane which causes the density in the stream to oscillate but does not appear to lead to any secular gap growth. Kicks along the orbit have the biggest effect since they impart the largest change in the kinetic energy, which changes the radial extent of the orbit and hence the orbital period. Since the orbital period is an increasing function of radius for any potential of astrophysical interest, particles which are kicked along their orbit have a longer period and fall behind the impact point. Likewise, particles which receive a kick opposite to their orbital direction have a shorter period and race ahead of the impact point.

Having established that the main effect of the velocity change the subhalo imparts is to kick stream particles towards the point of closest approach, it is straightforward to understand the three phases of gap formation. During the *compression phase*, the particles initially move towards the impact point which creates a density enhancement (2 of Fig. 1). After roughly an orbital period, the changes in orbital period reverse this motion and the gap enters the *expansion phase* where particles move apart (3 of Fig. 1), eventu-

ally forming a gap (4 of Fig. 1). Since the magnitude of the kick depends on position along the stream, particles will start to overtake each other at late times which will eventually lead to the *caustic phase* with particle pile-ups forming on either edge of the gap (5 of Fig. 1). As we will see below, one of the most important distinctions between the expansion phase and the caustic phase is that the gap growth slows from being linear in time to evolving as \sqrt{t} .

To complement the qualitative exposition above with quantitative analysis, we provide a roadmap of the pertinent figures and formulae. In Figure 7, Figure 8, and Figure 9 we show the density profiles of gaps in N-body simulations which exhibit the three phases of gap formation and can be accurately reproduced by our model. In Figure 4, we show an example of how the density in the center of the gap evolves in all three phases. In Figure 5, we show an example of how the gap size evolves for all times. In Figure 6, we show the density in the peaks around the gap during the intermediate phase. Lastly, we highlight some of the useful analytic results. The expression for gap size is given by (37) in the expansion phase and by (46) during the caustic phase. The expression for the central density is given by (39) and the expression for the peak density is given by (42).

3 RIGOROUS DERIVATION

Guided by the sketch of the gap growth process as presented in the previous section, let us now develop an analytic framework for studying the stream density evolution after an encounter with a subhalo. The derivation can be broken down into three main steps. First, we will use the impulse approximation to compute the velocity kicks the subhalo imparts along the stream. Next, we will compute the orbits which result from these velocity kicks. Finally, we will use these orbits to construct the stream density at all times, allowing us to examine the gap behavior in all three phases.

3.1 Orbit perturbation under the subhalo's impulse

The general setup for a subhalo flyby is shown in Figure 2 with the subhalo passing by the stream with an arbitrary geometry. We use a similar axis convention to that in Carlberg (2013) with the stream oriented in the y -direction, with x in the radial direction in the host potential, and with z perpendicular to the orbital plane. The stream is moving in the positive y -direction in a spherical potential $\phi(r)$, on a circular orbit with radius r_0 , with velocity $v_y = \sqrt{r_0 \partial_r \phi(r_0)}$. We consider a flyby of a subhalo which is moving in an arbitrary direction with velocity (w_x, w_y, w_z) which makes a closest approach at $(b_x, 0, b_z)$, where we have chosen our coordinates and origin so the closest approach occurs in the $x-z$ plane with the origin on the stream. Since the impact parameter and subhalo velocity are orthogonal at the point of closest approach, we can parameterize this point as $(b \cos \alpha, 0, b \sin \alpha)$ where $b = \sqrt{b_x^2 + b_z^2}$, and the subhalo velocity at closest approach as $(-w_\perp \sin \alpha, w_y, w_\perp \cos \alpha)$, where $w_\perp = \sqrt{w_x^2 + w_z^2}$. Finally, we define the relative velocity between stream and the subhalo along the stream, $w_\parallel = v_y - w_y$, and the magnitude of the total relative velocity, $w = \sqrt{w_\parallel^2 + w_\perp^2}$.

Let us now compute the velocity change along the stream from the passage of a Plummer sphere with mass M and scale radius r_s . For the duration of the flyby, we treat the stream as a straight line, translating at a constant velocity. In the limit that the velocity change is small relative to the orbital velocity, we can use the

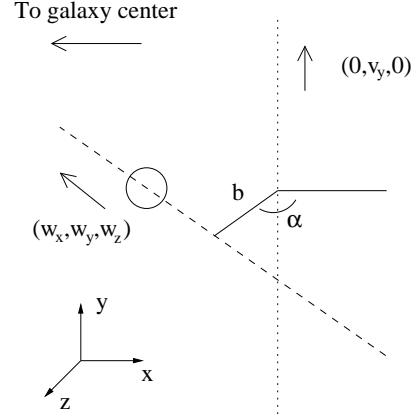


Figure 2. Our axis convention looking down on the stream. The dotted line is the stream and the dashed line is the path of the subhalo. The solid lines show the impact parameter, b , and its angle in the $x-z$ plane, α . The center of the host potential is to the left and the orbit is counterclockwise.

impulse approximation to get:

$$\begin{aligned} \Delta v_x &= \int_{-\infty}^{\infty} a_x dt \\ &= \int_{-\infty}^{\infty} \frac{GM(b_x + w_x t) dt}{\left((y + w_\parallel t)^2 + w_\perp^2 t^2 + b^2 + r_s^2\right)^{\frac{3}{2}}} \\ &= \frac{2GM(bw^2 \cos \alpha + yw_\perp w_\parallel \sin \alpha)}{w((b^2 + r_s^2)w^2 + w_\perp^2 y^2)}. \end{aligned} \quad (1)$$

Likewise we can compute the other two components of the velocity change, Δv_y and Δv_z :

$$\Delta v_y = -\frac{2GMw_\perp^2 y}{w((b^2 + r_s^2)w^2 + w_\perp^2 y^2)}, \quad (2)$$

$$\Delta v_z = \frac{2GM(bw^2 \sin \alpha - yw_\perp w_\parallel \cos \alpha)}{w((b^2 + r_s^2)w^2 + w_\perp^2 y^2)}. \quad (3)$$

In Figure 3 we show a schematic plot of the velocity kick along the stream, Δv_y , versus distance from the point of closest approach. As we will see below, the features of this relation, along with the resulting orbital motion, give rise to the rich dynamics of gap evolution.

Note that our assumption that the stream can be treated as a straight line implies that the region over which the velocity kick occurs, $\approx \frac{w}{w_\perp} \sqrt{b^2 + r_s^2}$, is much smaller than the radius of the orbit, r_0 . Furthermore, the assumption that the stream is translating at a constant velocity implies that the duration of the impact, $\approx \sqrt{b^2 + r_s^2}/w_\perp$, is much shorter than the orbital time, r_0/v_y . Therefore, we can only use these results i) for the substructure flybys reasonably close to the stream, ii) for the perturbers which are significantly smaller than the stream's orbital radius, and iii) for the perturbers moving sufficiently fast towards the stream, i.e. $\frac{w}{w_\perp} \frac{\sqrt{b^2 + r_s^2}}{r_0} \ll 1$ and $\frac{v_y}{w_\perp} \frac{\sqrt{b^2 + r_s^2}}{r_0} \ll 1$. Also note that these expressions for the velocity kicks are similar to those that appear in Yoon, Johnston & Hogg (2011) and Carlberg (2013) due to the similarity of the force from a Plummer sphere with that of a point mass at a given impact parameter.

Now that we have the amplitude of the kick in each direction

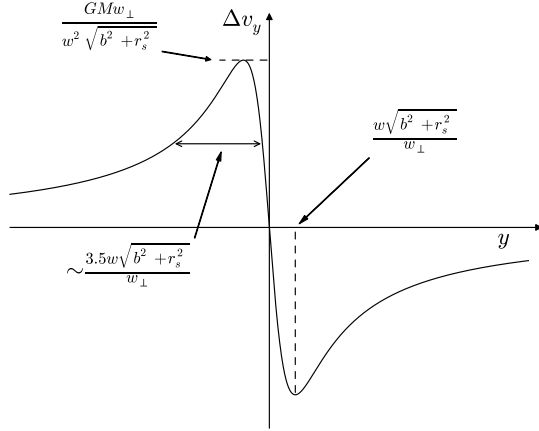


Figure 3. A schematic plot of the velocity kick along the stream, Δv_y , versus position along the stream, y . We have marked the distance of the maximum velocity kick from the point of closest approach, the size of the maximum velocity kick, and the width at half maximum. As we discuss in the text, the features of this relation, and the resulting orbital motion, give rise to the rich dynamics of gap formation.

$(\Delta v_x, \Delta v_y, \Delta v_z)$, we can compute the resulting orbit of each particle along the stream. In what follows, we carry out the analysis at leading order in $\frac{\Delta v}{v_y}$ and ignore terms that are $O(\frac{\Delta v^2}{v_y^2})$. After the kick, each particle finds itself in a new orbital plane defined by the angular momentum:

$$\begin{aligned} L_x &= 0, \\ L_y &= -r_0 \Delta v_z, \\ L_z &= r_0 v_y + r_0 \Delta v_y. \end{aligned} \quad (4)$$

This new orbital plane is rotated in the $y-z$ plane in the positive x direction by $\frac{\Delta v_z}{v_y}$. If we rotate our coordinates to align with this plane we find that the size of the velocity kick in the new x and y direction is unchanged at leading order in $\frac{\Delta v_y}{v_y}$ and $\frac{\Delta v_z}{v_y}$. As a result, the kick in the z direction tilts the orbital plane but otherwise leaves the orbit unchanged. This tilt varies along the stream and causes stream particles to oscillate in the z direction with an amplitude of $r_0 \frac{\Delta v_z}{v_y}$ with respect to the original plane. This small oscillation is in contrast to the secular growth of the stream gap along the orbit which we will see below. For the rest of the analysis, we will only consider the kicks in the x and y direction. As is customary to describe the orbit, i.e. the dependence of the particle's radius on the orbital phase, θ , we switch variables to $r = \frac{1}{u}$:

$$\frac{d^2 u}{d\theta^2} + u = -\frac{1}{L_z^2} \partial_u \phi. \quad (5)$$

This expression is then expanded to leading order around the original orbit, $u = u_0 + \Delta u$, with $u_0 = \frac{1}{r_0}$, taking first order expansions of the potential and L_z , to get

$$\frac{d^2 \Delta u}{d\theta^2} + \gamma^2 \Delta u = -2u_0 \frac{\Delta v_y}{v_y}, \quad (6)$$

where $\gamma^2 = 1 + \frac{u_0^2}{v_y^2} \partial_u^2 \phi(u_0^{-1})$. The solution to the above equation is

$$\Delta u = -\frac{2u_0 \Delta v_y}{v_y} \frac{(1 - \cos \gamma \theta)}{\gamma^2} - \frac{u_0 \Delta v_x}{v_y} \frac{\sin \gamma \theta}{\gamma}, \quad (7)$$

where we have imposed the conditions $\Delta u(0) = 0$ and $\partial_\theta \Delta u(0) = -u_0 \frac{\Delta v_x}{v_y}$ since the stream particle was initially on a circular orbit and received a velocity kick, Δv_x , in the radial direction. Re-writing (7) in terms of $r = r_0 + \Delta r$, and expanding at leading order in $\frac{\Delta r}{r_0}$, we get

$$\Delta r = \frac{2r_0 \Delta v_y}{v_y} \frac{(1 - \cos \gamma \theta)}{\gamma^2} + \frac{r_0 \Delta v_x}{v_y} \frac{\sin \gamma \theta}{\gamma}, \quad (8)$$

where we can re-write γ in terms of r :

$$\gamma^2 = 3 + \frac{r_0^2}{v_y^2} \partial_r^2 \phi(r_0). \quad (9)$$

Now that we know how the radius evolves after the perturbation, we can determine the particle's angular velocity using conservation of angular momentum:

$$L_z = r^2 \dot{\theta}. \quad (10)$$

After the impact, the angular momentum is given in (4), resulting in an angular rate of

$$\begin{aligned} \dot{\theta} &= \frac{v_y}{r_0} \left(1 + \frac{\Delta v_y}{v_y}\right) \left(1 + \frac{\Delta r}{r_0}\right)^{-2}, \\ &\approx \frac{v_y}{r_0} \left(1 + \frac{\Delta v_y}{v_y} - 2 \frac{\Delta r}{r_0}\right). \end{aligned} \quad (11)$$

This equation highlights the effect of the change in velocity as well as the change in radius on the angular velocity of the orbit. Note that if only the effect of the change in velocity is considered, no gaps will be produced as such perturbation leads only to a density enhancement since the Δv_y term kicks particles towards $y = 0$. Next we can use the expression for Δr from (8) in (11) to obtain

$$\dot{\theta} = \frac{v_y}{r_0} \left(1 - \frac{\Delta v_y}{v_y} \frac{4 - \gamma^2}{\gamma^2} + 4 \frac{\Delta v_y}{v_y} \frac{\cos \gamma \theta}{\gamma^2} - 2 \frac{\Delta v_x}{v_y} \frac{\sin \gamma \theta}{\gamma}\right). \quad (12)$$

Finally, the orbital equation for $\theta(t)$ at leading order in $\frac{\Delta v}{v_y}$ can be derived by re-arranging and integrating (12)

$$\theta(t) \left(1 + \frac{\Delta v_y}{v_y} \frac{4 - \gamma^2}{\gamma^2}\right) - 4 \frac{\Delta v_y}{v_y} \frac{\sin \gamma \theta(t)}{\gamma^3} + 2 \frac{\Delta v_x}{v_y} \frac{(1 - \cos \gamma \theta(t))}{\gamma^2} = \frac{v_y}{r_0} t. \quad (13)$$

This is a transcendental equation which can be solved numerically to give $\theta(t)$. However, since this analysis is at leading order in $\frac{\Delta v}{v_y}$, we can approximately solve this by switching variables to $\Delta \theta(t) = \theta(t) - \frac{v_y t}{r_0}$, and expand at leading order in $\frac{\Delta \theta(t)}{\frac{v_y t}{r_0}}$, to get

$$\Delta \theta(t) = -\frac{\Delta v_y t}{r_0} \frac{4 - \gamma^2}{\gamma^2} + \frac{4 \Delta v_y}{v_y} \frac{\sin(\frac{\gamma v_y t}{r_0})}{\gamma^3} - \frac{2 \Delta v_x}{v_y} \frac{(1 - \cos(\frac{\gamma v_y t}{r_0}))}{\gamma^2}, \quad (14)$$

which is valid as long as $\Delta \theta \ll \frac{v_y t}{r_0}$ and $\Delta \theta \ll \frac{\pi}{\gamma}$.

3.2 Stream evolution after the subhalo flyby

With the analytic solution given in (14), or a numerical solution to (13), we have a map from the positions of particles in the stream at

impact to their positions at any later time. If we consider a particle initially at position y relative to the impact point, i.e. at an angle $\psi_0 = \frac{y}{r_0}$ relative to the point of closest approach, the position of this particle at a later time, in coordinates which rotate with the unperturbed stream, is given by

$$\psi(\psi_0, t) = \psi_0 + \Delta\theta(\psi_0, t), \quad (15)$$

where we have added the label ψ_0 to both ψ and $\Delta\theta$ since the velocity kick from the subhalo depends on the initial position along the stream. In the rest of the work we will drop the ψ_0 argument in $\psi(t)$ to simplify the notation. Plugging the expression for $\Delta\theta(t)$ from (14) into (15) gives us an analytic formula for $\psi(t)$ in terms of the velocity kicks, $\Delta v_x, \Delta v_y$. Using the velocity kick amplitudes from (1) and (2) we find

$$\psi(t) = \psi_0 + \frac{f\psi_0 - g}{\psi_0^2 + B^2}, \quad (16)$$

where

$$f = \frac{4 - \gamma^2}{\gamma^2} \frac{t}{\tau} - \frac{4 \sin\left(\frac{\gamma v_y t}{r_0}\right)}{\gamma^3} \frac{r_0}{v_y \tau} - \frac{2\left(1 - \cos\left(\frac{\gamma v_y t}{r_0}\right)\right)}{\gamma^2} \frac{w_{\parallel}}{w_{\perp}} \frac{r_0}{v_y \tau} \sin \alpha, \quad (17)$$

$$g = \frac{2\left(1 - \cos\left(\frac{\gamma v_y t}{r_0}\right)\right)}{\gamma^2} \frac{b w_{\perp}^2 \cos \alpha}{r_0 w_{\perp}^2} \frac{r_0}{v_y \tau}, \quad (18)$$

$$B^2 = \frac{b^2 + r_s^2}{r_0^2} \frac{w_{\perp}^2}{w_{\perp}^2}, \quad (19)$$

and the timescale τ is given by

$$\tau = \frac{w r_0^2}{2GM}. \quad (20)$$

Note that f, g, B , and τ are independent of ψ_0 so although these formulae appear complicated, the map between ψ_0 and $\psi(t)$, (16), is quite simple in terms of ψ_0 . In the work below, we will do many expansions at late time where f and g are dominated by the leading term in f , so we also define

$$f_L = \frac{4 - \gamma^2}{\gamma^2} \frac{t}{\tau}, \quad (21)$$

which is the leading order behavior of f at late times.

The map between ψ_0 and $\psi(t)$, (15), allows us to immediately compute the stream density at time t . If the map is single valued, the density at $\psi = \psi(t)$ is given by

$$\rho(\psi, t) = \rho_0(\psi_0) \left| \frac{d\psi(t)}{d\psi_0} \right|^{-1}, \quad (22)$$

where $\rho_0(\psi_0)$ is the initial density profile of the stream. If the map is not single valued, i.e. once the stream particles pass each other, we must sum the right hand side over all ψ_0 which map to ψ . Plugging the map from ψ_0 to $\psi(t)$, (16), into the density expression we get

$$\frac{\rho(\psi, t)}{\rho_0} = \left(1 + \frac{fB^2 - f\psi_0^2 + 2g\psi_0}{(\psi_0^2 + B^2)^2} \right)^{-1}. \quad (23)$$

Note that (16) and (23) parametrically define the gap profile at all times and for all impact geometries. This gives us a functional form for the gap profile which is very general and can be quickly computed. This can be used as a realistic match filter to find gaps in observations (i.e. Carlberg, Grillmair & Hetherington 2012).

As detailed below, after the flyby the evolution of the

stream density changes behaviour several times. Let us define the timescales which describe the phases of this metamorphosis. First, there is the timescale for a radial oscillation which can be read off from the expression for $\Delta\theta(t)$, (14). We will call this the orbital timescale:

$$t_{\text{orbital}} \equiv \frac{r_0}{v_y \gamma}. \quad (24)$$

Next, we have the timescale for kicked particles to reach the impact point. Since particles at the origin receive no kick, when kicked particles located further away along the stream reach the impact point, they will form a caustic. This timescale is given by the distance to the particle which receives the largest kick, $\frac{w_{\perp}}{w_{\perp}^2} \sqrt{b^2 + r_s^2}$, divided by the size of the kick it receives, $\frac{GM w_{\perp}}{w_{\perp}^2 \sqrt{b^2 + r_s^2}}$ (see Fig. 3). The onset of the early caustic happens after

$$t_{\text{early caustic}} \equiv \frac{w_{\perp}^3}{w_{\perp}^2} \frac{b^2 + r_s^2}{GM}. \quad (25)$$

Lastly, we have the timescale for the particle which received the largest kick to reverse its motion towards the impact point and reach particles which received a negligible kick. The estimate is similar to the case for the early caustic but now there is the added complication of the orbital motion. This is captured in the leading term of (14) where we see that the velocity is effectively boosted by a factor of $\frac{4 - \gamma^2}{\gamma^2}$. Therefore, in the expansion phase, the caustics will form after approximately

$$t \sim \frac{\gamma^2}{4 - \gamma^2} \frac{w_{\perp}^3}{w_{\perp}^2} \frac{b^2 + r_s^2}{GM}, \quad (26)$$

Note that the caustic timescale is derived more rigorously in Section 3.4 and is given by (34).

We note that while this derivation is quite general, we have made several assumptions for the impulse approximation to hold. As we argued in the discussion after (3), our derivation of the velocity kicks assumes that the stream can be treated as a straight line which implies $\frac{w_{\perp}}{w_{\perp}^2} \frac{\sqrt{b^2 + r_s^2}}{r_0} \ll 1$. Comparing this with the expression for B , (19), we see that this constraint is equivalent to $B \ll 1$. Furthermore, if we compare the expressions for f and g , ((17), (18)), we see that g is smaller than the leading term in f by a factor on the order of $B \frac{w_{\perp}}{w_{\perp}^2} \frac{r_0}{v_y \tau}$ and smaller than the subleading terms by a factor on the order of $B \frac{w_{\perp}}{w_{\perp}^2}$. In our analysis below, we will assume that w and w_{\perp} are the same order of magnitude so that we have $g \ll f$.

We will now analyze the consequences of these results and build a quantitative picture of the qualitative description in Figure 1 and Section 2.

3.3 Early Time Behavior: Compression Phase

At early times, $t \ll t_{\text{orbital}}$, the map between ψ_0 and $\psi(t)$ simplifies to

$$\psi(t) = \psi_0 + \frac{\Delta v_y t}{r_0}, \quad (27)$$

i.e. particles translate along the stream at the velocity with which they have been kicked. In terms of quantities defined above, this becomes

$$\psi(t) = \psi_0 - \frac{t}{\tau} \frac{\psi_0}{\psi_0^2 + B^2}. \quad (28)$$

Since $\frac{d\psi(t)}{dt}$ and ψ_0 have opposite signs, the stream will compress. As we have discussed earlier, this is expected since the effect of the

subhalo's passage is to pull particles towards the point of closest approach. Note that this compression does not depend on the details of the potential, it depends solely on the details of the impact by the subhalo.

To characterise the stream compression, we define the center of the perturbation as the location of the density extremum, $\frac{d\rho}{d\psi} = 0$, which gives $\psi_0 = 0$. Therefore, the central density is

$$\rho(0, t) = \left(1 - \frac{t}{B^2\tau}\right)^{-1}. \quad (29)$$

Thus we see that the central density increases at early times. Once the time is on the order of the orbital time, the picture is slightly more complicated. In general, the center of the gap is given by the particles with $\psi_0 \approx \frac{g}{3f}$. However, since we are only interested in the leading order behavior of the density, and we have restricted ourselves to the $g \ll f$ regime, we will take $\psi_0 = 0$ to be the center. This gives a central density of

$$\rho(0, t) = \left(1 + \frac{f}{B^2}\right)^{-1}. \quad (30)$$

Consequently, the compression reaches a maximum when $\frac{df}{dt} = 0$, i.e.

$$\frac{4 - \gamma^2}{\gamma^2} - \frac{4 \cos\left(\frac{\gamma v_{\text{yt}}}{r_0}\right)}{\gamma^2} - \frac{2 \sin\left(\frac{\gamma v_{\text{yt}}}{r_0}\right)}{\gamma} \frac{w_{\parallel}}{w_{\perp}} \sin \alpha = 0. \quad (31)$$

The solution to this equation will be on the order of $\frac{r_0}{\gamma v_{\text{yt}}}$, i.e. the compression phase lasts on the order of a radial period, t_{orbital} . After this time, the particles will reverse direction due to changes in the period, leading to the expansion phase where the density decreases, eventually forming a gap.

In Figure 4, we compare the central density in our model to the central density in an N-body simulation of a particle bundle and find good agreement. The N-body simulation is described in Section 4.1. The setup is a stream-like structure on a circular orbit with a radius of 30 kpc around a point mass with $M = 2.5 \times 10^{11} M_{\odot}$. The subhalo, with $M = 10^7 M_{\odot}$ and $r_s = 250$ pc, directly impacts the stream with a velocity of 100 km/s perpendicular to the stream's orbital plane. In Figure 4 we see that during the early part of the compression phase, the density increases linearly as expected from (29), and eventually reaches a maximum density after approximately 100 Myr. After this, the expansion phase begins.

Apart from the density enhancement, there is one more interesting feature during the compression phase. Since the stream particles are initially kicked towards the point of closest approach, it is possible that the stream particles will pass each other and form caustics before the change in period leads to the expansion phase. This will happen if the orbital timescale is sufficiently long compared to the timescale for stream particles to reach the origin, i.e. the early caustic timescale. We can determine when caustics are present when the map between ψ_0 and $\psi(t)$ is multivalued, i.e. when $\frac{d\psi(t)}{d\psi_0} = 0$ has real solutions. In general, this gives a quartic equation for which the conditions for real roots are relatively simple but not very enlightening. However, if we restrict to early times, $t \ll t_{\text{orbital}}$, the constraint for caustics to form simplifies to

$$t_{\text{orbital}} \gg B^2\tau, \quad (32)$$

which we can re-write as

$$t_{\text{orbital}} \gg \frac{1}{2} t_{\text{early caustic}}, \quad (33)$$

confirming our intuition that a long orbital time is needed to form caustics in this phase. Note that this caustic can be seen in the pole of the density in the early phase, (29).

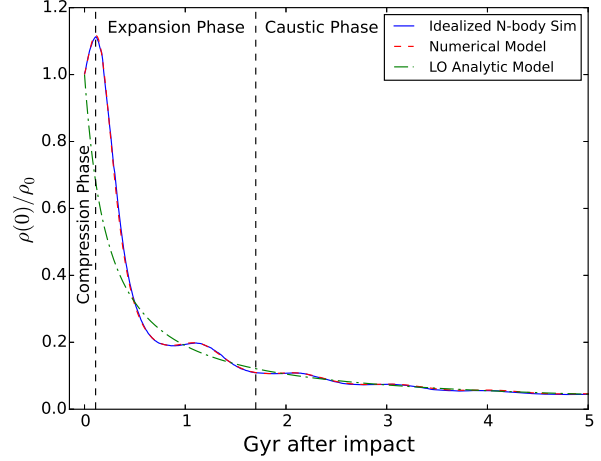


Figure 4. Central density as a function of time in a Keplerian potential. The solid blue line shows the result of an N-body simulation (described in Sec. 4.1), the dashed red curve shows the result of the model when the central density is computed from a numerical solution for the density profile using (13), and the solid green curve shows the result when the late time (leading order) behavior of f is used in (30). The numerical model reproduces the results from the N-body simulation and the leading order analytical model reproduces the right trends but has no epicyclic motion. The compression phase lasts approximately 100 Myr in this example, after which the expansion phase begins.

3.4 Intermediate Time Behavior: Expansion Phase

A quick tug from the passing subhalo changes the orbital period of particles in the stream. Even though the particles are immediately attracted towards the impact point, with time, the orbital phase offset due to period change accumulates and reverses the compression, leading to a runaway gap expansion. This expansion phase continues until eventually density caustics form as the kicked particles catch up with more distant particles that received negligible kicks. We can determine this time by finding the time when the map between ψ_0 and $\psi(t)$ becomes multivalued, i.e. when $\frac{d\psi(t)}{d\psi_0} = 0$ has real solutions. This occurs at $f \approx 8B^2$ and if $g = 0$, this condition is exact. This sets a timescale for the onset of caustics, and hence the end of the expansion phase:

$$t_{\text{caustic}} \approx \frac{4\gamma^2}{4 - \gamma^2} \frac{w_{\perp}^3}{w_{\perp}^2} \frac{b^2 + r_s^2}{GM}. \quad (34)$$

Note that this is very similar to the timescale described in Section 3, save for the additional factor of 4. Also note that it is possible for caustics to be present during the early part of the expansion phase if they were created in the compression phase. These caustics will last until $f \gtrsim -B^2$, where the condition is exact if $g = 0$.

During the expansion phase, a gap forms near the point of closest approach. Figure 1 shows a schematic of the density profile of the stream during the compression and expansion phase. There are three obvious quantities of interest: the gap size, the density in the center of the gap, and the density of the peak. We will now compute each of these.

After the compression stage and before the caustics form, we can write down the density at all positions using (23). We define the gap size as the size of the region within which there is an underdensity, i.e. the region within which $\frac{d\psi(t)}{d\psi_0} > 1$. The boundaries

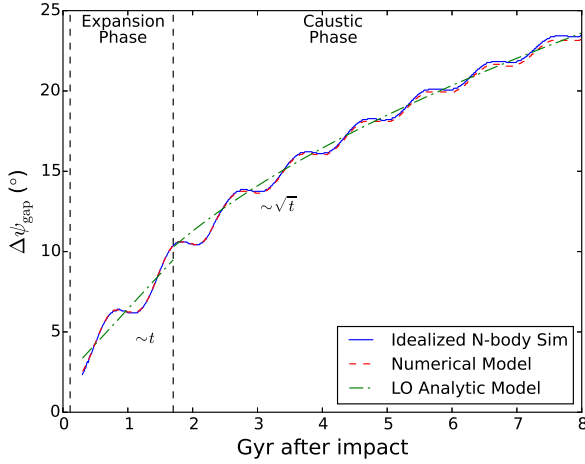


Figure 5. Size of the gap as a function of time in a Keplerian potential. The solid blue curve shows the result of an N-body simulation (described in Sec. 4.1), the dashed red curve shows the result of the model when the gap size is computed from a numerical solution for the density profile using (13), and the solid green curve shows the result when the late time (leading order) behavior of f is used in (37) and (46). The early phase is not shown here since there are no gaps in that phase. The expansion phase with a linear growth lasts until approximately 1.7 Gyr in this example. After that, caustics form and the gap grows like \sqrt{t} .

of this region are given by particles with

$$\psi_0 = \frac{g}{f} \pm B \sqrt{1 + \frac{g^2}{B^2 f^2}}. \quad (35)$$

In the limit that $f \gg g$, we can further simplify this and plugging into the map from ψ_0 to $\psi(t)$, (16), we find the leading behavior of the gap size:

$$\Delta\psi_{\text{gap}}(t) = 2B + \frac{f_L}{B}. \quad (36)$$

Note that if $g = 0$, the leading order f_L in this expression can be replaced with the full f expression. Plugging in for f_L we get

$$\Delta\psi_{\text{gap}}(t) = 2 \frac{w}{w_\perp} \frac{\sqrt{r_s^2 + b^2}}{r_0} + \frac{2GMw_\perp}{w^2 r_0 \sqrt{r_s^2 + b^2}} \frac{4 - \gamma^2}{\gamma^2} t. \quad (37)$$

As is obvious from this equation, the stream gap grows linearly with time in this phase. In addition to this linear growth, there is an epicyclic behavior which causes the gap size to oscillate as it grows. In Figure 5 we show an example of how the gap size grows, where the epicyclic motion is clearly visible. The simulation setup for this example is described in Section 3.3.

The density in the center of the gap is identical to the density during the compression phase:

$$\frac{\rho(0, t)}{\rho_0} = \left(1 + \frac{f}{B^2}\right)^{-1}. \quad (38)$$

This is the general result but we can determine the overall trend by taking the leading term in f once again to get:

$$\frac{\rho(0, t)}{\rho_0} = \left(1 + \frac{4 - \gamma^2}{\gamma^2} \frac{w_\perp^2}{w^3} \frac{2GM}{b^2 + r_s^2} t\right)^{-1}. \quad (39)$$

Thus we see that the density in the center goes like t^{-1} at late times.

Finally, we can compute the position and density of the peaks

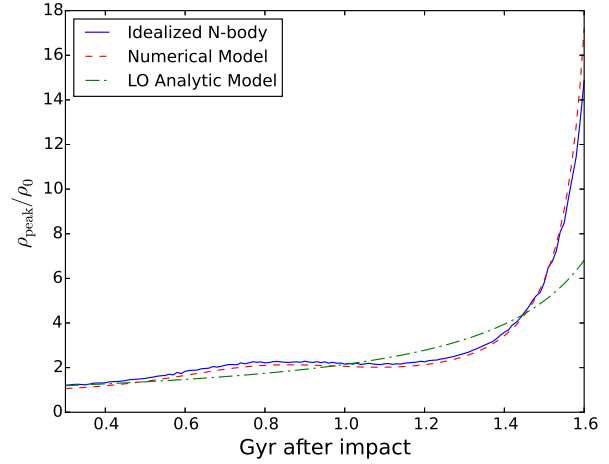


Figure 6. Peak density as a function of time during the expansion phase. The solid blue line shows the result of an N-body simulation (described in Sec. 4.1), the dashed red curve shows the result of the model when the peak density is computed from a numerical solution for the density profile using (13), and the solid green curve shows the result when the late time (leading order) behavior of f is used in (42). The early and late phases are not included in this plot because there is no peak in the early phase and because there are caustics in the late phase. Note that the simulation gives a consistently higher density until ~ 1.4 Gyr after impact because we are taking the maximum of a density which is a realization with a finite number of particles.

around the gap. We compute these by finding the zeros of $\frac{d\rho}{d\psi}$, which gives the constraint

$$2f\psi_0(\psi_0^2 - 3B^2) - 2g(3\psi_0^2 - B^2) = 0. \quad (40)$$

In the limit $f \gg g$, we can neglect the second term and we see that the density peaks are at $\psi_0^2 = 3B^2$. Plugging this back into the density at late times we find

$$\frac{\rho_{\text{peak}}(t)}{\rho_0} = \left(1 - \frac{f_L}{8B^2}\right)^{-1}. \quad (41)$$

Note that if $g = 0$, the f_L in this expression can be replaced with f . Plugging in the expression for f_L , we find

$$\frac{\rho_{\text{peak}}(t)}{\rho_0} = \left(1 - \frac{1}{8} \frac{4 - \gamma^2}{\gamma^2} \frac{w_\perp^2}{w^3} \frac{2GM}{b^2 + r_s^2} t\right)^{-1}. \quad (42)$$

The density diverges as we approach t_{caustic} , heralding the formation of caustics. We show an example of the peak density in Figure 6 which shows the asymptotic behavior. As before, the simulation setup for this example is described in Section 3.3.

3.5 Late Time Behavior: Caustic Phase

At late times, $t > t_{\text{caustic}}$, stream particles overtake each other and four caustics form, two on either side of the gap. Figure 7 shows the evolution of the stream density profile around the gap with caustics in a Keplerian potential. There are several interesting properties we can compute: the size of the gap, the relative strength of the caustics, the distance between the two caustics on either side of the gap, and the characteristic width of each caustic.

The locations of these caustics comes from determining where $\frac{d\psi(t)}{d\psi_0} = 0$. At late times, these caustics correspond to the particles

with

$$\psi_{0,\text{inner}}^2 = f_L, \quad (43)$$

and

$$\psi_{0,\text{outer}}^2 = B^2, \quad (44)$$

where the labels refer to the caustic position relative to the impact point during the caustic phase. We can then plug these into the map between ψ_0 and $\psi(t)$, (16), to determine their positions:

$$\begin{aligned} \psi_{\text{inner}}(t) &= \pm 2\sqrt{f_L}, \\ \psi_{\text{outer}}(t) &= \pm \left(B + \frac{f_L}{2B} \right). \end{aligned} \quad (45)$$

Thus, comparing with (36) and (37) we see the outer caustic moves linearly in time and continues at the same rate as the gap edge during the expansion phase. In addition, there is an inner caustic which moves proportionally to \sqrt{t} . As we will see below (also see Fig. 7), the inner caustic is both stronger and wider than the outer caustic. Thus the inner caustic sets the gap size in this phase:

$$\Delta\psi_{\text{gap}}(t) = 4 \left(\frac{4 - \gamma^2}{\gamma^2} \frac{2GM}{wr_0^2} t \right)^{\frac{1}{2}}. \quad (46)$$

Figure 5 shows the gap size evolution during the caustic phase. We see that the model closely matches the N-body simulation. Similarly, Figure 4 shows the density in the center of the gap during the caustic phase and once again reveals good agreement with the N-body simulation.

Another useful prediction during this phase is the relative strengths of the inner and outer caustics which are proportional to $\left| \frac{d^2\psi(t)}{d\psi_0^2} \right|^{-\frac{1}{2}}$ evaluated at the caustic position,

$$\frac{\rho_{\text{inner}}(t)}{\rho_{\text{outer}}(t)} = \frac{f_L^{\frac{3}{4}}}{2B^{\frac{3}{4}}}. \quad (47)$$

Thus we see that the inner caustic dominates the outer caustic for $t \gg t_{\text{caustic}}$.

The distance between the inner and outer caustic is another interesting quantity since it gives the size of the overdensity region around the gap. This bump size is given by

$$\Delta\psi_{\text{bump}} = B + \frac{f_L}{2B} - 2\sqrt{f_L}. \quad (48)$$

Finally we note that these caustics can be extremely narrow. Their characteristic widths are given by $\left| \frac{d^2\psi(t)}{d\psi_0^2} \right|^{-1}$ evaluated at the caustic. At late times, the widths of the inner and outer caustic are given by:

$$\Delta\psi_{\text{inner}} \approx \frac{\sqrt{f_L}}{4}, \quad (49)$$

$$\Delta\psi_{\text{outer}} \approx \frac{B^{\frac{3}{2}}}{2\sqrt{f_L}}. \quad (50)$$

Thus we see that the width of the inner caustic grows with time while the width of the outer caustic shrinks (as illustrated in Figure 7).

4 COMPARISON WITH SIMULATIONS

To demonstrate the validity of the derivation above we have carried out several N-body simulations. These simulations were all run with the pure N-body part of GADGET-3 which is closely related to GADGET-2 (Springel 2005).

4.1 Idealized Simulations

The first set of simulations we carried out are similar to those in Carlberg (2013) and mimic the setup of the derivation above. We placed 10^6 massless tracer particles on a short arc (0.6 radians) on a circular orbit with $r_0 = 30$ kpc and a circular velocity of $v_y = 190$ km/s. These arcs were evolved in three different potentials: NFW (Navarro, Frenk & White 1997), Keplerian, and spherical harmonic oscillator (SHO). The NFW has a mass of $M = 10^{12} M_\odot$, a concentration of $c = 15$, and a scale radius $R_s = 14.0$ kpc. The parameters of the Keplerian and SHO potential were chosen to have the same circular velocity as the NFW potential at 30 kpc, resulting in a mass of $2.5 \times 10^{11} M_\odot$ for the Keplerian potential, and a spring constant of $k = 40 \text{ km}^2/\text{s}^2/\text{kpc}^2$ for the SHO potential.

We modified GADGET to include a subhalo particle which moves at a constant velocity and feels no force but exerts a Plummer force on the other particles. This was done to mimic the setup of the toy model and avoid any complications arising from orbit of the subhalo. The subhalo particle has a velocity of $w_z = 100$ km/s and exerts a Plummer force with $M = 10^7 M_\odot$ and $r_s = 250$ pc. The initial conditions for the subhalo particle and the stream particles were setup so that the impact would occur in the middle of the stream, i.e. a direct impact perpendicular to the stream's orbital plane.

Figure 8 shows the stream density profiles in simulations with three different potentials at several epochs. As we saw in the derivation above, the gap evolution in each potential is controlled by γ , (9). The NFW potential has $\gamma^2 = 2$, the Keplerian potential as $\gamma^2 = 1$, and the SHO potential has $\gamma^2 = 4$. The streams in all three potentials show a density enhancement at early times. Note that the compression phase is identical for all three potentials since the early behavior is independent of potential. The compression is followed by an expansion phase and in the NFW and Keplerian potentials, the expansion phase results in gap growth. As expected from the expression for the gap size, (37), the gap grows three times faster in the Keplerian potential. Interestingly, there is no secular gap growth in the SHO potential since the orbital period in a SHO is independent of radius. Instead, the stream oscillates between an overdensity and an underdensity.

The caustic phase is not visible in Figure 8 but we have shown the caustic phase for the Keplerian potential in Figure 7. We see that the model correctly predicts the locations of the double caustics on either side of the gap, as well as the density profile of the gap. The reason we do not show the NFW potential in Figure 7 is that it will not have entered the caustic phase by the final panel of Figure 7. As we can read off from the caustic timescale, (34), the caustic timescale for the NFW potential is three times longer than the caustic timescale for the Keplerian potential.

Additionally, several properties of the stream gaps in the Keplerian potential are compared against the predictions of our model. Namely, Figure 4 shows the central density in the intermediate and late phase, Figure 5 gives the gap size, and Figure 6 presents the density of the peaks around the gap in the intermediate phase. In all cases, we find good agreement between the simulation and the model.

4.2 Realistic Simulation

In the previous section, we compared the analytical model to simulations of an interaction of a subhalo with a stream consisting of particles on the same circular orbit. In realistic streams produced through tidal disruption, the debris particles would have a distribu-

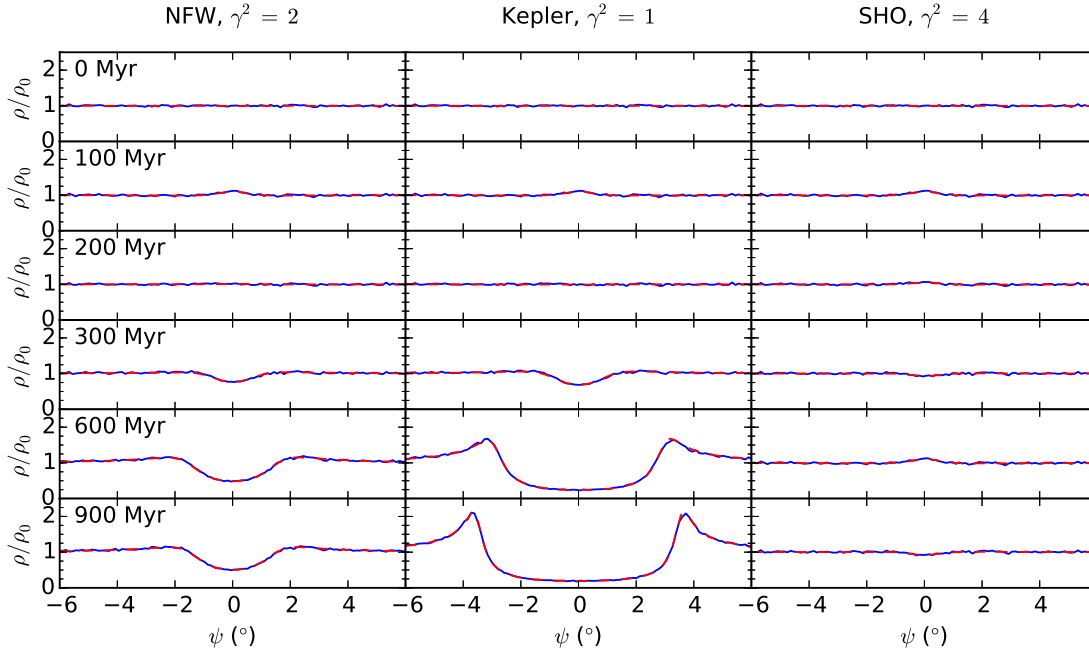


Figure 8. Density profile of the stream after an impact in three different host potentials. The left panel is for an NFW host, the middle panel is for a Keplerian host, and the right panel is for a simple harmonic oscillator host. The solid blue curve shows the result of an N-body simulation and the dashed red curve shows the prediction from the model using a numerical solution of (13). As described in the text, the gap grows three times faster in the Keplerian potential than the NFW potential in the expansion phase. In addition, gaps do not grow in the SHO potential since the period is independent of radius.

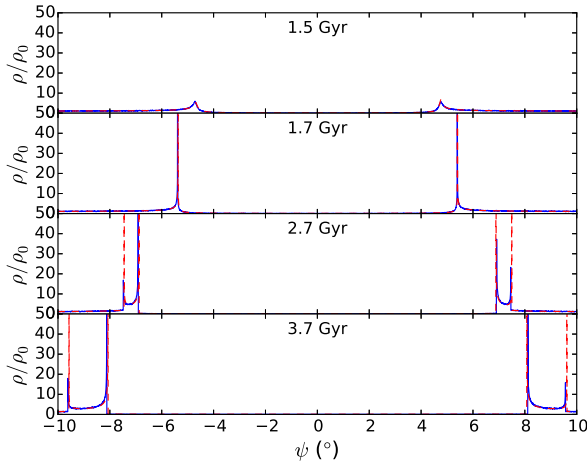


Figure 7. Evolution of caustics at late time for the Keplerian potential. The solid blue curve shows the result of an N-body simulation and the dashed red curve shows the prediction from the model using a numerical solution of (13). The caustics in this example form roughly 1.7 Gyr after impact.

tion of energies and angular momenta. Moreover, the progenitor of the stream is constantly being stripped resulting in particles which can potentially fill in the gap. To show that our simple model is still useful for gaps in a realistic streams, we have carried out a N-body simulation where we have a subhalo directly impact a tidal stream generated by disrupting a globular cluster.

We model the globular cluster as a Plummer sphere with a mass of $2.5 \times 10^5 M_\odot$ and a scale radius of 8 pc. It is placed on a circular orbit of radius 10 kpc around an NFW potential with

$M = 10^{12} M_\odot$, with $c = 15$ and $R_s = 14.0$ kpc. The Plummer sphere is represented with 10^6 particles which have a smoothing length of 0.43 pc. This smoothing length is used to minimize the force errors (Dehnen 2001). The Plummer sphere is evolved for 3 Gyr and in this time a long cold stream with a length of $\sim 180^\circ$ is produced. As described above, we add a subhalo particle which moves with a fixed velocity and exerts a Plummer force, with $M = 10^8 M_\odot$ and a scale radius of $r_s = 250$ pc, on all other particles. This particle is setup to impact the center of the leading arm of the stream, which corresponds to a radius of 9.77 kpc, at 100 km/s perpendicular to the orbital plane. We then follow the evolution of the stream for 4 Gyr after the impact to see how the stream evolves. Note that we have slightly modified the setup in Section 4.1, using a more massive halo on an orbit with a smaller radius, to make the gap more pronounced.

For our analytic model, we assume the stream particles are on a single circular orbit with $r_0 = 9.77$ kpc and use the circular velocity at this radius, 168.2 km/s, for the stream velocity. We also have to account for the fact that the unperturbed stream now has a non-trivial density profile. This is naturally included in our model since the density is related to the initial density through (22). Note that before the halo flyby, the stream has developed a broad density enhancement close to the end of the stream (top panel of Fig. 9). This is a consequence of the fact that the Plummer sphere we inserted on a circular orbit is initially out of equilibrium with the tidal field and has a stripping rate which is a decreasing function of time. This results in a peak of the density along the stream. We chose to directly impact this peak to avoid any additional confusion in interpreting density peaks not created by the gap.

Figure 9 shows the density profile along the stream at various times. We see the same behavior as we found in Section 3: there is an initial density enhancement which gives rise to a gap with peaks around it. The caustics which were prominent in the toy

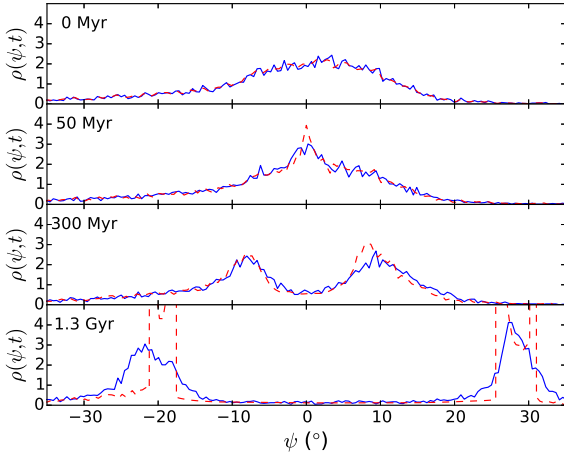


Figure 9. Evolution of the stream density in an N-body simulation of a subhalo impact on a stream produced by disrupting a Plummer sphere. The solid blue curve shows the result of an N-body simulation and the dashed red curve shows the prediction from the model using a numerical solution of (13).

model (Fig. 7) are now mostly smoothed over by the dispersion in E-L of the stream debris and by the non-trivial shape of the initial density profile. In the lowermost panel, we see that there are some small bumps near where the caustics should be. While these bumps are marginally visible in many of the snapshots at the correct location, it is unclear if we are actually resolving them.

Figure 10 illustrates how the gap size evolves and reports a fairly good agreement between the result of the realistic N-body simulation and our model. We see that despite the lack of the distinctive caustic features, the gap size growth starts off linear and then slows to be proportional to \sqrt{t} , in agreement with our model. One possible reason for a small discrepancy with the N-body result having a slightly steeper slope than our model is likely due to the fact that the stream is not on a single circular orbit, as we have assumed, but rather the particles sample a sequence of orbits which are stretching away from the progenitor due to the difference in angular momentum and hence period. This causes the unperturbed stream to stretch out which will increase the rate of gap growth.

Figure 11 compares the density in the center of the gap in the N-body simulation against our model. Overall, we find a very good agreement at early times, but our model slightly underpredicts the density at late times. This is likely due to the stream particles filling in the gap since they have a spread in energy and angular momentum, an effect not included in our model. Due to this dispersion, the gap can be filled by material which is stripped from the progenitor at a later time.

Figure 12 gives the on-sky picture of the stream as viewed from the center of the galaxy. Since the subhalo is moving perpendicular to the orbital plane, the stream particles receive a kick in that direction which causes the stream particles to oscillate perpendicular to the orbital plane. However, the main effect is for the stream to stretch out along the orbital direction.

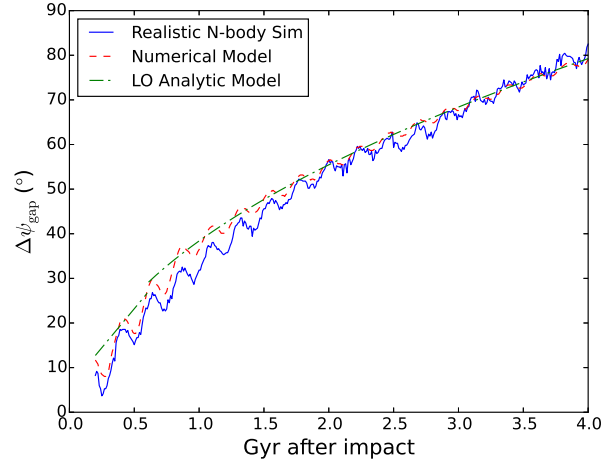


Figure 10. Gap size in an N-body simulation of a disrupting Plummer sphere. The solid blue curve shows the result of an N-body simulation, the dashed red curve shows the result of the model when the gap size is computed from a numerical solution for the density profile using (13), and the solid green curve shows the result when the late time (leading order) behavior of f is used in (37) and (46).

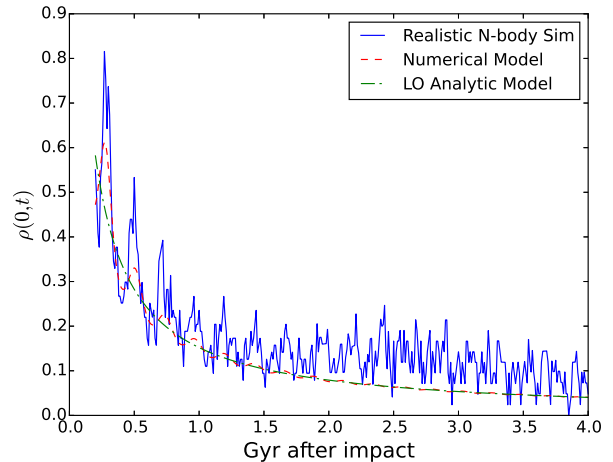


Figure 11. Density in the center of the gap as a function of time. The solid blue curve shows the result of an N-body simulation, the dashed red curve shows the result of the model when the central density is computed from a numerical solution of the density using (13), and the solid green curve shows the result when the late time behavior of f is used in (29). We see that our model reproduces the density at early times but underpredicts it at late times. This is likely due to stream particles filling the gap due to their distribution in energy and angular momentum.

5 EXTRACTING PHYSICAL PARAMETERS FROM GAPS

Now that we understand how the growth of stream gaps depends on the host potential and the properties of the subhalo, let us elucidate the inverse problem: given the gap properties, can useful constraints be placed on the properties of the subhalo? To answer this question, we first have to think about the observables of the gap. These observables depend on the phase the gap is in. During the compression phase, the only feature is the density enhancement. While

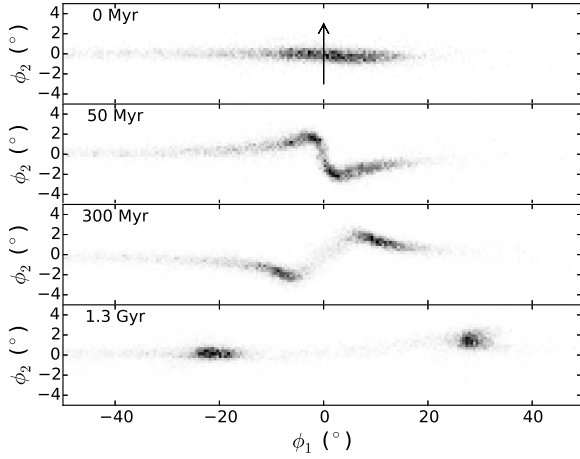


Figure 12. Stream resulting from the disruption of a Plummer sphere as viewed from the center of the galaxy at different times. ϕ_1 is aligned with the orbital plane of the unperturbed stream. The times in the top left show the time since impact. The arrow shows the motion of the subhalo which impacts the stream at $\phi_1 = 0$ at $t = 0$. Due to the geometry of this particular encounter, the stream oscillates out of the orbital plane. However, the main effect of the subhalos passage is the formation of a gap which grows like \sqrt{t} , as in Fig. 10.

this feature potentially presents a useful constraint on the subhalo flyby properties, it is unlikely this phase will be observable due to its short lifetime. During the expansion phase, the simplest set of observables would be the size of the gap, the density in the center of the gap, and the density in the peaks around the gap. During the caustic phase, the observables would be the size of the gap, the relative strength of the caustics, the distance between caustics, and the width of the caustics. Alternatively, we could attempt to fit the gap profile with the parametric form of the density profile. We will discuss both approaches below. For clarity of the following discussion, we re-write f_L and B^2 since these two parameters control the overall behavior of observables mentioned above

$$f_L = \frac{4 - \gamma^2}{\gamma^2} \frac{2GM}{wr_0^2} t, \quad (51)$$

$$B^2 = \frac{b^2 + r_s^2}{r_0^2} \frac{w^2}{w_\perp^2}. \quad (52)$$

As we saw in Section 3.4, in the expansion phase, the gap size is governed by the quantities B and f_L/B , however at late times the second term is significantly larger than the first and is responsible for the growth. As a result, we can think of the gap size as controlled by the combination f_L/B . We also found that the density of the peak and trough is controlled by f_L/B^2 . Therefore, for a given gap size, the density contrast increases as B decreases. In Figure 13, we demonstrate this with an example of three gaps which are identical in size but have different density contrasts. The setup is identical to the setup above: the stream is on a circular orbit with $r_0 = 30$ kpc, around a NFW with $M = 10^{12} M_\odot$, $c = 15$, and $R_s = 14.0$ kpc. The fiducial subhalo is a Plummer sphere with $M = 10^7 M_\odot$, $r_s = 250$ pc, and $w_\perp = 100$ km/s. Note that the density profiles in Figure 13 occur at different times in the different setups since we require the gaps to have the same size. Thus, we see that by measuring the gap size and the density contrast we can constrain f_L and B .

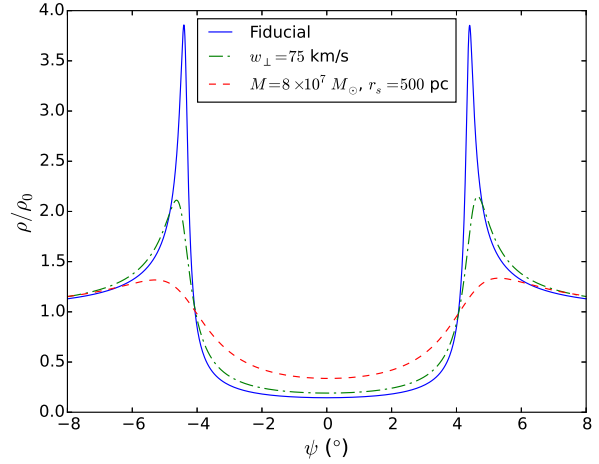


Figure 13. The density profile for various flybys which have the same gap size but different profiles. The fiducial setup is for a subhalo with a mass of $10^7 M_\odot$, a scale radius of 250 pc, and a perpendicular velocity, w_\perp , of 100 km/s. As discussed in the text, for a given gap size, the density contrast increases as B decreases. As a result, for a given gap size, a smaller perpendicular velocity, w_\perp , results in a smaller density contrast. Similarly, for a given gap size, a more massive and more extended subhalo results in a smaller density contrast.

In the late phase, the argument is similar, except now the gap size goes like $\sqrt{f_L}$ and the size of the overdense region around the gap depends on B and f_L as in (48). As a result, we can once again constrain f_L and B . This argument extends to the other properties during the caustic phase, i.e. the relative strength of the caustics and their width, which also depend on combinations of f_L and B .

5.1 Degeneracy for Single Gap

Given that the gap size and the density contrast only depend on two quantities, f_L and B , we see that there will be a large degeneracy when inferring subhalo properties. If we assume that we know the orbital properties of the stream, i.e. r_0 and v_y , as well as the host potential, γ , we see that the gap properties depend on 7 quantities: $M, r_s, b, w_\perp, w_\parallel, \alpha, t$. These 7 quantities are constrained by f_L , B , and a constraint on the density of the subhalo, $\frac{M}{r_s}$. Thus we are left with four unconstrained degrees of freedom.

This picture is further complicated by the epicyclic motion which causes the gap size and the density to oscillate (i.e. Fig. 4, Fig. 5). As a result, when these properties are measured, there will be some uncertainty about exactly what phase of the expansion they are in.

In the best case scenario, we could fit the stream density profile with the parametric function for the stream density ((16) and (23)). Looking at these equations, we see that this parametric function only depends on f , g , and B . Therefore, even if we fit the exact stream profile, we will be left with a three dimensional degeneracy. This means that it is not possible to uniquely infer the properties of a subhalo from a gap profile, even in the most optimistic case.

5.2 Constraints from Gap Spectrum

This gloomy prediction may improve somewhat if we instead try to model the spectrum of gaps created by multiple encounters with

subhalos. For a statistical sample of gaps, we could use additional information to constrain the distribution of velocities and impact parameters using constraints on the position and velocity distributions of the subhalos from N-body simulations. The gap spectrum would then allow us to potentially constrain the subhalo mass function. Note that this analysis would be complicated by overlapping gaps as well as the epicyclic overdensities expected in streams, e.g. Küpper, MacLeod & Heggie (2008).

6 DISCUSSION

6.1 Generalizations

In the work above, we have built a model for gaps formed by the flyby of a Plummer sphere near a stream on a circular orbit. While this model contains many simplifying assumptions, the qualitative picture we have developed holds for more generic encounters. The three distinct phases, as well as the transition from a gap which grows linearly in t to one which grows like \sqrt{t} , will be present in the flybys of generic subhalos near streams on non-circular orbits whose particles have a distribution of energies and angular momenta.

The generalization to different subhalo density profiles affects the resulting velocity kicks, $(\Delta v_x, \Delta v_y, \Delta v_z)$. For a general spherically symmetric subhalo profile, these kicks must be evaluated numerically. However, as long as the kicks produced have the same qualitative features as the ones generated by a Plummer sphere, i.e. a similar shape in the plane of velocity change versus distance from the point of closest approach (i.e. as in Fig. 3), the qualitative picture will remain true. For example, for an NFW profile, the radial force does not go to zero as we approach the origin. As a result, the velocity kick for particles near the impact point will change rapidly along the stream (i.e. making Fig. 3 steeper near the origin), making it much easier for caustics to form in the compression phase. This can be understood in terms of the early caustic timescale which is the distance to the largest kick, divided by its amplitude. However, the intermediate and late time behavior will still be the same since they are due to the change in the orbital period and the particles with the largest kick catching up to those which received a negligible kick. Note that these differences are even smaller for impact parameters larger than the scale radius of the impactor since then the precise profile becomes unimportant.

The extension to eccentric orbits is non-trivial for a general potential since the orbits are not analytic. However, the qualitative picture in Section 2 holds for non-circular orbits so we expect the same overall behavior seen here. For eccentric orbits, the gap size will oscillate more dramatically as it grows due to the difference in angular velocity from pericenter to apocenter. In addition, the effect of the subhalo's passage will also depend on where along the orbit the closest approach occurs. For a fixed kick size, a kick at pericenter will have a larger effect on the kinetic energy and hence the period compared to a kick at apocenter. However, this simple picture is complicated by the fact that both the stream particles and the subhalo will likely have a lower velocity at the stream's apocenter, resulting in a larger kick at apocenter. Despite these complications, as we show in Section 6.4, the scaling behaviors of the gap size reproduce what is seen in cosmologically motivated suite of simulations by Yoon, Johnston & Hogg (2011). In addition, N-body simulations (not shown here) of eccentric orbits around NFW potentials show the same qualitative behavior with an overdensity at early times, leading to a gap, and finally to caustics at late times.

The extension to streams with a distribution of energy and angular momenta was shown in the N-body simulation in Section 4.2 where we first generated a stream by disrupting a Plummer sphere, and then generated a gap with the flyby of another Plummer sphere. Despite the realistic distribution in energy and angular momentum, the gap size growth still exhibits the linear growth in t in the expansion phase and the \sqrt{t} growth in the caustic phase (Fig. 10). In addition, there is a density enhancement visible at early times (Fig. 9).

6.2 Dependence on Potential

To develop some intuition about how the gap size growth depends on the potential we consider the power-law potential, $\phi = Ar^n$, which would imply that $\gamma^2 = 2 + n$. Plugging this into the expressions for the gap size ((37) or (46)) we find that the growth rate is proportional to $\frac{2-n}{2+n}$ during the expansion phase and $\sqrt{\frac{2-n}{2+n}}$ during the caustic phase. Therefore, as n approaches -2 the gap grows faster and faster. This follows from the fact that the effective potential, $\phi(r) + \frac{L^2}{2r^2}$, expanded around the radius for a circular orbit, becomes flatter and flatter in this limit and thus the radial oscillations get larger. Since the period is an increasing function of radius for potentials with $n < 2$, these radial oscillations lead to dramatically different periods and hence a rapidly expanding gap. As n approaches 2, the gap grows more slowly since it is approaching a spherical harmonic oscillator where the period is independent of radius and no gap will form, as shown in Figure 8.

6.3 Simplified Picture

In Section 2 and Section 3 we gave a qualitative and a rigorous derivation of how gaps grow. These results can be summarised quite neatly. The formation of gaps is governed by three timescales: the orbital timescale, t_{orbital} , the early caustic timescale, $t_{\text{early caustic}}$, and the caustic timescale, t_{caustic} . Within an orbital timescale, the stream will compress, expand, and then begin to form a gap. If $t_{\text{early caustic}} \ll t_{\text{orbital}}$, early caustics will form in the compression phase and vanish before the expansion phase. Between the orbital timescale and the caustic timescale the stream gap will grow linearly in time. After the caustic timescale, caustics form on the leading edge of the gap and the gap size goes like \sqrt{t} . In terms of B and the caustic timescale, the gap size and densities are also remarkably simple. In the intermediate phase, the gap size is given by

$$\Delta\psi_{\text{gap}} = 2B + 8B \frac{t}{t_{\text{caustic}}}, \quad (53)$$

the density of the peaks around the gap is given by

$$\frac{\rho_{\text{peak}}(t)}{\rho_0} = \left(1 - \frac{t}{t_{\text{caustic}}}\right)^{-1}, \quad (54)$$

and the density in the center of the gap (which holds in the intermediate phase and the late phase) is given by

$$\frac{\rho(0, t)}{\rho_0} = \left(1 + \frac{8t}{t_{\text{caustic}}}\right)^{-1}. \quad (55)$$

During the late phase, the gap size is given by

$$\Delta\psi_{\text{gap}} = 8\sqrt{2}B\sqrt{\frac{t}{t_{\text{caustic}}}}. \quad (56)$$

Thus we see that the stream properties are especially simple when expressed in terms of t_{caustic} and B . For example, we can immediately see that if a gap has a very small density in the center,

$\rho/\rho_0 < 0.1$, the gap is in the caustic phase and the gap size is growing as \sqrt{t} .

6.4 Comparison with Previous Work

In this work, we have extended the results of Carlberg (2013) to the formation of gaps in arbitrary host potentials and to subhalos which are Plummer spheres. As in that work, we use the impulse approximation to compute the kick on stream particles from the passage of a subhalo. In Carlberg (2013), the effect on the stream is computed analytically using guiding centers and epicyclic motion for the case of a logarithmic potential. The results found in Carlberg (2013) match the qualitative behavior in the expansion phase of this work with a gap size that grows linearly in time. However, our results differ from those in Carlberg (2013) since the expression for the gap size in that work (Equation 16 of Carlberg 2013) has a different scaling behavior with larger mass subhalos giving smaller gap sizes and also appears to have typographical errors since the units are inconsistent. In addition, we find a richer structure with three phases of gap formation and a different gap growth at late times. Note that there are hints of the three phases of gap formation in Figure 6 of Carlberg (2013) which shows the shape of the stream in an N-body simulation, where x is the radial direction and y is the tangential direction along the orbit. Projections of these curves onto the y axis give the density along the stream. Although the curves are not labeled by their time, the early density enhancement is visible from the curves which are steep near $y = 0$. In addition, projections of the saw-tooth shape in that figure give the caustics described in this paper.

The results of this work can be used to shed light on the results of N-body simulations of stream impacts in previous works. For example, in Carlberg (2012), N-body simulations are used to determine the density in the center of a gap from impacts with various mass subhalos and impact parameters. This central density is then used to make cuts on what mass subhalos and impact parameters would create observable gaps. In Carlberg (2012), fits were made to the central density as a function of mass and impact parameter but we now have an analytic expression for this result, i.e. (39), which matches this behavior. However, we note that our analysis is for flybys of Plummer spheres while Carlberg (2012) uses spherical Hernquist profiles (Hernquist 1990).

Similarly, in Yoon, Johnston & Hogg (2011), the authors show the results of N-body simulations of stream impacts with NFW subhalos of varying mass (Figure 6 of that work). The caustic timescale for their fiducial simulation is 800 Myr so for the snapshots presented, the fiducial run is well into the caustic phase. At the bottom panel of their Figure 6, we see the effect of varying the mass. In the caustic phase, the gap size is given by (46), where it goes like \sqrt{M} . Thus, if we increase the mass by a factor of 10, the gap size should increase by a factor of 3, as seen in their figure. If we decrease the mass by a factor of 10, the gap is now in the intermediate phase but the gap will still be roughly 1/3 of the fiducial gap size, as seen in their figure. This can be repeated for the other panels to understand the quantitative trends seen.

7 CONCLUSION

In this work, we have studied how gaps are created in tidal streams by the close passage of a dark matter subhalo. We restricted our analysis to streams on circular orbits which allowed us to tackle

the problem analytically. Our main results can be summarised as follows.

- We provide a parametric expression for the stream density ((16) and (23)). We emphasize that this result allows one to determine the stream density at all times, for an arbitrary impact geometry and an arbitrary spherically symmetric potential. This can be used to make realistic matched filters for finding gaps in observed streams. We also note that this model can easily be extended to different subhalo profiles by computing the velocity kicks and the parametric function numerically.
- We confirm that gap formation in tidal streams is a runaway process which can lead to dramatic density reduction across tens of degrees on the sky. However, as we show explicitly for the first time, the orbital perturbation inflicted by the subhalo depends on the shape of the effective potential around the impact point. Therefore, the rate of gap growth depends strongly on the mass distribution in the host galaxy: in extreme cases, e.g. in a spherical harmonic oscillator potential, the gaps will not develop at all.
- We discover that the evolution of gaps in tidal streams proceeds in three distinct phases. First, there is a *compression phase* since the subhalo pulls stream particles towards the point of closest approach. These kicks change the orbital period of each stream particle leading to the *expansion phase*, which causes the compression to reverse, and eventually leading to the creation of a gap. Due to the change in the orbital period, stream particles which received large kicks will eventually pass those which received no kick, leading to the *caustic phase* with caustics (particle pile-ups) on either side of the gap. We predict therefore four caustics altogether, each pair with a different behaviour as a function of time.
- Our analytic model allows us to make quantitative predictions for each phase. During all phases, we have an expression for the central density of the gap. During the expansion phase, we have expressions for the gap size and the density in the peaks around the gap. During the caustic phase, we have expressions for the gap size, relative strength of the caustics, distance between the caustics, and width of the caustics.
- Contrary to previous work, we unravel an important change in the gap growth at late times. Stream gaps stop growing as fast as t and switches to a slower rate proportional to \sqrt{t} as the *expansion phase* evolves into the *caustic phase*.
- In addition to the secular behavior described above, we demonstrate that the gap properties oscillate during all three phases due to epicyclic motion. These oscillations will become yet more pronounced for streams on eccentric orbits and, unfortunately, are bound to muddle any inference based on the gap properties.
- We verified the analytical model with N-body numerical experiments. These include a set of idealized simulations with stream particles on circular orbits and found an almost perfect match with the gap profile, as well as the gap size, central density, and peak density. In addition, we compared the model to an N-body simulation where a globular cluster on a circular orbit is disrupted to create a realistic stream. In this case, again the model describes the gap properties rather well, with a slight mismatch at late times, likely due to the spread in energy and angular momentum in the stream.
- Finally, we take advantage of the analytic model to see how observations of gap profiles can be used to constrain the dark matter subhalo properties. When considering a single gap, we found a large degeneracy between the subhalo properties, the gap properties, the host potential and the epoch of observation. Even in the best case scenario when the entire gap profile can be matched, it is

not possible to uniquely infer the properties of the subhalo and the geometry of the flyby.

Let us stress once again that this qualitative picture outlined above is quite general and will hold for other dark matter subhalo profiles, non-circular orbits, and streams with a realistic distribution of energy and angular momentum. The analytic expressions presented in this work also allow us to quantitatively understand the trends seen in N-body simulations of stream disruptions with varying impactors (i.e. Yoon, Johnston & Hogg 2011; Carlberg 2012). While our study has uncovered many degeneracies and complications inherent in the stream spatter analysis, we have built a solid framework which can be used to infer dark matter subhalo properties from tidal stream gaps.

Lastly, we have made two movies to showcase the different phases of gaps described in this work. The first movie shows the gap produced in the realistic simulation described in Section 4.2 and can be found here¹. The second movie shows a gap produced using the same setup but with a smaller subhalo with $M = 10^7 M_\odot$ and $r_s = 125$ pc and can be found here².

ACKNOWLEDGEMENTS

We thank the anonymous referee for a helpful and thorough report. We thank the Streams group at Cambridge for stimulating discussions and in particular we thank Wyn Evans for detailed comments on this manuscript, as well as Sergey Koposov and Jason Sanders for useful discussions. In addition, DE thanks Kerbal Space Program for invaluable intuition gained from practicing orbital maneuvers. The research leading to these results has received funding from the European Research Council under the European Union's Seventh Framework Programme (FP/2007-2013)/ERC Grant Agreement no. 308024.

REFERENCES

- Belokurov V., Evans N. W., Irwin M. J., Hewett P. C., Wilkinson M. I., 2006, *ApJ*, 637, L29
 Bernard E. J. et al., 2014, *MNRAS*, 443, L84
 Bonaca A., Geha M., Kallivayalil N., 2012, *ApJ*, 760, L6
 Carlberg R. G., 2009, *ApJ*, 705, L223
 Carlberg R. G., 2012, *ApJ*, 748, 20
 Carlberg R. G., 2013, *ApJ*, 775, 90
 Carlberg R. G., Grillmair C. J., 2013, *ApJ*, 768, 171
 Carlberg R. G., Grillmair C. J., Hetherington N., 2012, *ApJ*, 760, 75
 Dalal N., Kochanek C. S., 2002, *ApJ*, 572, 25
 Dehnen W., 2001, *MNRAS*, 324, 273
 Diemand J., Kuhlen M., Madau P., Zemp M., Moore B., Potter D., Stadel J., 2008, *Nature*, 454, 735
 Grillmair C. J., Dionatos O., 2006, *ApJ*, 643, L17
 Hernquist L., 1990, *ApJ*, 356, 359
 Ibata R. A., Lewis G. F., Irwin M. J., Quinn T., 2002, *MNRAS*, 332, 915
 Johnston K. V., Spergel D. N., Haydn C., 2002, *ApJ*, 570, 656

- Koposov S. E., Irwin M., Belokurov V., Gonzalez-Solares E., Yoldas A. K., Lewis J., Metcalfe N., Shanks T., 2014, *MNRAS*, 442, L85
 Küpper A. H. W., MacLeod A., Heggie D. C., 2008, *MNRAS*, 387, 1248
 Navarro J. F., Frenk C. S., White S. D. M., 1997, *ApJ*, 490, 493
 Odenkirchen M. et al., 2003, *AJ*, 126, 2385
 Siegal-Gaskins J. M., Valluri M., 2008, *ApJ*, 681, 40
 Springel V., 2005, *MNRAS*, 364, 1105
 Springel V. et al., 2008, *MNRAS*, 391, 1685
 Vegetti S., Koopmans L. V. E., Bolton A., Treu T., Gavazzi R., 2010, *MNRAS*, 408, 1969
 White S. D. M., Rees M. J., 1978, *MNRAS*, 183, 341
 Yoon J. H., Johnston K. V., Hogg D. W., 2011, *ApJ*, 731, 58

¹ Available through MNRAS and <http://youtu.be/MXfKmnARBNM>

² Available through MNRAS and <http://youtu.be/p0kqH510x3M>